

A Late-time Radio Survey of Type Ia-CSM Supernovae with the Very Large Array

OLIVIA GRIFFITH,¹ GRACE SHOWERMAN,¹ SUMIT K. SARBADHICARY,^{2,3,4,5} CHELSEA E. HARRIS,¹ LAURA CHOMIUK,¹
JESPER SOLLERMAN,⁶ PETER LUNDQVIST,⁶ JAVIER MOLDÓN,⁷ MIGUEL PÉREZ-TORRES,^{7,8} ERIK C. KOOL,^{6,9,10} AND
TAKASHI J. MORIYA^{11,12,13}

¹Center for Data Intensive and Time Domain Astronomy, Department of Physics and Astronomy, Michigan State University, East Lansing, MI 48824, USA

²Department of Physics, The Ohio State University, Columbus, Ohio 43210, USA

³Center for Cosmology & Astro-Particle Physics, The Ohio State University, Columbus, Ohio 43210, USA

⁴Department of Astronomy, The Ohio State University, Columbus, Ohio 43210, USA

⁵Department of Physics and Astronomy, The Johns Hopkins University, Baltimore, MD 21218 USA

⁶The Oskar Klein Centre, Department of Astronomy, Stockholm University, AlbaNova, SE-10691, Stockholm, Sweden

⁷CSIC, Instituto de Astrofísica de Andalucía, Glorieta de la Astronomía S/N, E-18008, Granada, Spain

⁸School of Sciences, European University Cyprus, Diogenes street, Engomi, 1516 Nicosia, Cyprus

⁹Finnish Centre for Astronomy with ESO (FINCA), University of Turku, 20014 Turku, Finland

¹⁰Department of Physics and Astronomy, University of Turku, 20014 Turku, Finland

¹¹National Astronomical Observatory of Japan, National Institutes of Natural Sciences, 2-21-1 Osawa, Mitaka, Tokyo 181-8588, Japan

¹²Graduate Institute for Advanced Studies, SOKENDAI, 2-21-1 Osawa, Mitaka, Tokyo 181-8588, Japan

¹³School of Physics and Astronomy, Monash University, Clayton, VIC 3800, Australia

ABSTRACT

Type Ia-CSM supernovae (SNe) are a rare and peculiar subclass of thermonuclear SNe characterized by emission lines of hydrogen or helium, indicative of a high-density circumstellar medium (CSM). Their implied mass-loss rates of $\sim 10^{-4} - 10^{-1} M_{\odot} \text{ yr}^{-1}$ (assuming $\sim 100 \text{ km s}^{-1}$ winds) from optical observations are generally in excess of values observed in realistic SN Ia progenitors. In this paper, we present an independent study of CSM densities around a sample of 29 archival Ia-CSM SNe using radio observations with the Very Large Array at 6 GHz. Motivated by the late ($\sim 2 \text{ yr}$) radio detection of the Ia-CSM SN 2020eyj, we observed old ($> 1 \text{ yr}$) SNe where we are more likely to see the emergent synchrotron emission that may have been suppressed earlier by free-free absorption by the CSM. We do not detect radio emission down to 3σ limits of $\sim 35 \mu\text{Jy}$ in our sample. The only radio-detected candidate in our sample, SN 2022esa, was likely mis-classified as a Ia-CSM with early spectra, and appears more consistent with a peculiar Ic based on later-epochs. Assuming a wind-like CSM with temperatures between $2 \times 10^4 \text{ K}$ and 10^5 K , and magnetic field-to-shock energy fraction (ϵ_B) = 0.01–0.1, the radio upper limits rule out mass-loss rates between $\sim 10^{-4} - 10^{-2} M_{\odot} \text{ yr}^{-1}$ (100 km s^{-1})⁻¹. This is somewhat in tension with the estimates from optical observations, and may indicate that more complex CSM geometries and/or lower values of ϵ_B may be present.

1. INTRODUCTION

The progenitor scenarios for Type Ia supernovae (SNe Ia) remain one of the biggest open questions in astrophysics. The two broad scenarios explored by the community have been the single degenerate scenario, involving a white dwarf accreting from a non-degenerate main-sequence star, red giant, or helium star companion (e.g. Whelan & Iben 1973; Nomoto 1982), and the double-

degenerate scenario, involving two white dwarfs in a binary system (e.g. Tutukov & Yungelson 1979; Iben & Tutukov 1984; Webbink 1984; Shen et al. 2018). Unfortunately, observations have yet to establish which combination of these scenarios are contributing to the observed SN Ia population in the universe (see e.g. Jha et al. 2019; Liu et al. 2023; Ruiter & Seitzzahl 2025, for recent reviews). Considering the importance of SNe Ia as the primary producers of Fe-group elements (Raiteri et al. 1996), as drivers of chemical enrichment in the universe (Matteucci & Recchi 2001), and as standard candles (e.g., Pskovskii 1977; Phillips 1993) for pre-

cise astrophysical distance measurements (Phillips 1993; Riess et al. 1998; Perlmutter et al. 1999; Phillips et al. 1999; Burns et al. 2018), the resolution of the SN Ia progenitor problem remains a high-priority goal for our field.

Here we focus on a particularly intriguing and rare sub-class of SNe Ia that have eluded explanation – SNe Ia-CSM (Silverman et al. 2013). They are characterized by strong narrow emission lines of hydrogen which have been attributed to circumstellar material (CSM) produced by mass-loss from the progenitor. SNe Ia-CSM also appear to be more luminous than normal SNe Ia, and have a preference for star-forming host galaxies (Sharma et al. 2023). They have been considered strong candidates for the single-degenerate channel, since white dwarfs with red-giant or asymptotic giant branch (AGB) star companions can have strong winds (e.g. Han & Podsiadlowski 2006; Dilday et al. 2012). Some well-known examples of Ia-CSM SNe include PTF11kx (Dilday et al. 2012), SN 2002ic (Hamuy et al. 2003) and SN 2005jg (Aldering et al. 2006). Many of them were previously confused with Type IIn SNe owing to dilution and blending of key spectral features by the bright continuum (Fox et al. 2015; Leloudas et al. 2015; Inserra et al. 2016). In very rare cases, CSM interaction can exhibit at late-times in SNe Ia due to distant, detached shells of CSM (e.g. Graham et al. 2019; Wang et al. 2024; Terwel et al. 2025; Mo et al. 2025).

A major conundrum of SNe Ia-CSM is that their implied mass-loss rates from the H-emission lines are typically in the range of $10^{-4} - 10^{-2} M_{\odot} \text{ yr}^{-1}$ (assuming wind velocities of 100 km s^{-1} , e.g. Aldering et al. 2006; Dilday et al. 2012; Silverman et al. 2013; Sharma et al. 2023). These are 2 – 4 orders of magnitude higher than observed in realistic single-degenerate progenitors with the highest mass-loss rates, such as symbiotic systems with AGB companions (e.g. Seaquist & Taylor 1990; Seaquist et al. 1993; Chomiuk et al. 2012a). Other scenarios such as dense shells of swept-up mass from recurrent novae (e.g. Moore & Bildsten 2012; Darnley et al. 2019), or common-envelope shells preceding formation of double-degenerate systems (e.g. Livio & Riess 2003) have also been invoked, but a clear connection between observations and progenitors is lacking so far for SNe Ia-CSM.

An orthogonal way of studying CSM properties is with radio observations, which trace synchrotron emission from SN shocks interacting with the ambient medium (Chevalier 1982). Given the observed luminosity or upper limits, and some assumptions about the fractional shock energy shared with the electrons and magnetic fields, reasonable estimates of the CSM density can

be obtained. While radio emission has been observed in many core-collapse SNe interacting with the dense CSM around their massive progenitors (e.g., Weiler et al. 2002; Chevalier et al. 2006; Soderberg et al. 2012), similar emission has been elusive in Type Ia SNe. Their non-detections have provided strong evidence that most SNe Ia have low-density environments, ruling out symbiotic companions, and even a substantial parameter space of nova-driven and accretion-disk-driven winds (e.g., Panagia et al. 2006; Chomiuk et al. 2012b, 2016; Horesh et al. 2012; Lundqvist et al. 2020; Harris et al. 2023).

In contrast to the general SN Ia population, there are fewer constraining radio observations of Ia-CSM SNe. Chomiuk et al. (2016) carried out the largest radio survey of SNe Ia, in which there were six Ia-CSM SNe that all showed non-detections. However, these observations were generally taken within a few months of the explosion, and therefore could have missed the radio emission due to synchrotron self-absorption and free-free absorption by the ionized CSM. This is clearly seen in radio observations of their closest counterparts, Type IIn SNe, whose radio light curves peak a few years after explosion (Chandra 2018; Bietenholz et al. 2021; Sfaradi et al. 2025). Unfortunately, very few late-time radio observations of SNe Ia-CSM exist on these timescales to detect emission and independently constrain the properties of the high density CSM.

In this paper, we present the first and largest “late-time” (i.e. $>1 \text{ yr}$ after explosion) radio survey of SNe Ia-CSM with the Very Large Array. The survey was inspired by the discovery of radio emission from the He-rich Ia-CSM, SN 2020eyj, which at a distance of $\sim 131 \text{ Mpc}$ produced bright radio emission ($\sim 10^{27} \text{ erg s}^{-1} \text{ Hz}^{-1}$) at 5–6 GHz on timescales of $\sim 1.5\text{--}2 \text{ yrs}$ after explosion (Kool et al. 2023). This is the first and only thermonuclear SN to date with detected radio emission, and together with the late-time radio emission in Type IIn SNe, encourages a similar search of Ia-CSM SNe, sufficiently late in time to detect any emergent emission. We targeted 29 archival SNe Ia-CSM with ages of at least 1 yr, and analyzed them with synchrotron emission models of interaction with a $\rho \propto r^{-2}$ wind-like CSM, in order to obtain constraints on their mass-loss rates, enabling comparison with values deduced from optical observations. The exact ages and distances for each SN are recorded in Table 1.

The paper is organized as follows: Section 2 describes the VLA observations of our 29 targets. Section 3 discusses the radio light curve model used for deriving mass-loss rates (or upper limits) from the observed luminosities. Section 4 goes over the results of our observations and measurements of mass-loss rates, and Section

5 discusses these in the context of mass-loss rate measurements from other wavelengths, and implications.

2. OBSERVATIONS

In this section, we describe the radio observations conducted on our SNe Ia-CSM sample. We observed 29 SNe Ia-CSM at 6 GHz with the Very Large Array (VLA) in the A configuration between July-Aug 2023 as part of the program VLA/23A-328 (PI: Sarbadhicary).¹ The sample was selected from published SNe Ia-CSM in [Silberman et al. \(2013\)](#) and [Fox et al. \(2015\)](#), and transients classified as “Ia-CSM” in the Transient Name Server for SNe Ia discovered after 2016. We excluded SNe Ia-CSM that are outside the declination limit of the VLA ($\delta > -35^\circ$). Our final sample consists of SNe with ages of 1 to 25 years, and are located at distances ranging from 90 to 900 Mpc (Table 1).

Our targets were primarily observed for 10 minute durations (a few distant ones for 20 and 30 minutes) in C-band (4 – 8 GHz), using continuum mode, which covers the entire 4 GHz of bandwidth with 2 MHz-wide channels. Observations were obtained in A-configuration to achieve good localization accuracy (with restoring beams of $\sim 0.3''$) and diminish the effects of diffuse emission from the SN host galaxies. Each target was observed between complex gain calibration observations lasting 1-2 minutes using calibrators that were selected for their brightness, high positional accuracy, and proximity to each respective target. Flux calibrations lasting ~ 8 minutes were done at the beginning of each observing block using one of the following of the VLA’s primary calibrators: 3C286, 3C138, 3C48, or 3C147.

We imaged and measured radio flux densities (or upper limits) for all of the targets in the sample using standard calibration and imaging procedures for radio continuum data followed in previous papers (e.g. [Chomiuk et al. 2016](#); [Harris et al. 2023](#); [Hosseinzadeh et al. 2023](#)). We follow the standard VLA calibration pipeline implemented in CASA version 6.4.1.12 ([CASA Team et al. 2022](#)) for reducing the continuum data from these observations. The pipeline applies online flags reported during observation, and additional flagging of RFI is done with the `rflag` algorithm. The pipeline performs iterative flagging–calibration cycles on the raw visibility data. The primary calibrators are used for delay, bandpass, and absolute flux density calibration, while the secondary calibrator is used for antenna-based complex gain calibrations. After the pipeline runs, each cal-

ibrated dataset was manually inspected and flagged for any remaining RFI.

Imaging is performed using the `tclean` task in CASA. We used `gridded=wproject` to mitigate the impact of non-coplanar baselines and sky curvature during wide-field imaging. For deconvolution, we used multi-term multi-frequency synthesis with `nterms=2` to account for frequency-dependent brightness in the imaging field. We applied Briggs weighting with `robust=0` to balance point source sensitivity with sidelobe contamination in our observations. We created images 6000 pixels wide, at a pixel scale of $0.07''$, which is approximately one-fifth of the synthesized beamwidth in VLA C-band and A-configuration. We cleaned our images for a maximum of 10^4 iterations or until the image root mean square contrast (RMS) was less than five times the peak residual (`nsigma=5`). No self-calibration was necessary as our final images were close to the expected noise limit, with no artifacts from bright sources.

For each object in our sample, we recorded the pixel flux density and the 3σ RMS noise at the location of the SN. Most of the SNe were non-detections, so we recorded 3σ upper limits at 6 GHz, defined as the flux density at the SN location plus the 3σ RMS noise in the 50-by-50 pixel region around the SN. If the flux density at the SN location was negative, we considered the 3σ RMS noise as the upper limit.

The majority of our sources turned out to be non-detections down to the 3σ limits of $\sim 35 \mu\text{Jy}$ reported in Table 1. The implications of these non-detections regarding progenitor mass loss rates are discussed in Section 4. One of our SNe, 2022esa, did produce detectable radio emission of $\sim 1.1 \text{ mJy}$, although as we discuss in Section 4, the TNS classification of this object as a Ia-CSM is likely dubious. In order to confirm that the radio emission at the location of SN 2022esa is transient in nature, we obtained follow-up observations in the same frequency and array configuration as part of VLA/24B-381. The dataset was flagged, calibrated and imaged following the same procedure as the VLA/23A-328 datasets discussed above. We additionally recorded the peak flux density of the point source in both images using elliptical gaussian fitting with the CASA task `imfit`. Indeed, the flux density of the source decreased to 0.8 mJy after a year, corresponding to a 30% decrease. These measurements are also presented in Table 1, and implications of the detections are further discussed in Section 4.

3. RADIO LIGHT CURVE MODEL

In this section, we describe our model of synchrotron radio emission due to SN-CSM interaction, which will

¹ Four of the SNe proposed in our program – SN 2005jg, 2005JG, 2013I, 2021admm – were part of a scheduling block that did not get observed during the 2023A semester as a result of C-priority.

Table 1. Radio Observations of our SN Ia-CSM sample.

SN Name	Discovery Date (UT)	Observation Date (UT)	Time Since Explosion (Years)	RA (J2000) (h:m:s)	Dec (J2000) (° :′ :″)	Distance (Mpc)	3 σ Flux Upper Limit (mJy)	3 σ Luminosity Upper Limit (10 ²⁵ erg s ^{−1} Hz ^{−1})
SN 1999E	99/01/15	23/08/20	24.6	13:17:16.37	−18:33:13.4	109.1	0.036	52.06
SN 2002ic	02/11/13	23/08/28	20.8	01:30:02.55	21:53:06.9	296.8	0.029	309.42
SN 2008cg	08/05/05	23/08/25	15.3	15:54:15.15	10:58:25.0	159.3	0.041	125.63
SN 2009in	09/08/25	23/08/27	14.0	23:22:35.32	−13:05:43.6	103.3	0.033	42.65
PTF10htz	10/04/03	23/08/16	13.4	13:08:37.52	79:47:13.2	153.9	0.048	136.72
SN 2011dz	11/06/26	23/08/25	12.2	16:12:44.82	28:17:03.2	106.9	0.037	51.17
SN 2011jb	11/11/28	23/08/13	11.7	11:37:04.80	15:28:14.2	382.5	0.034	593.60
CSS120327	12/03/27	23/08/20	11.4	11:05:20.08	−01:52:05.2	415.4	0.039	800.88
SN 2013dn	13/06/14	23/08/27	10.2	23:37:45.74	14:42:37.1	250.9	0.030	224.46
SN 2014T	14/02/22	23/08/25	9.5	14:36:04.98	02:20:34.2	411.5	0.033	667.66
SN 2014Y	14/03/02	23/07/30	9.4	07:23:33.38	54:26:19.8	172.0	0.028	99.06
SN 2014ab	14/03/09	23/08/20	9.5	13:48:05.99	07:23:16.4	101.2	0.040	49.68
SN 2016iks	16/11/20	23/08/27	6.8	23:07:21.53	02:54:28.2	282.7	0.026	252.19
SN 2016jae	16/12/22	23/08/13	6.6	09:42:34.51	10:59:35.4	91.4	0.036	35.74
SN 2017eby	17/04/01	23/08/25	6.4	14:38:50.74	14:44:26.0	368.1	0.030	494.09
SN 2017ifu	17/10/28	23/08/28	5.8	02:50:55.03	−02:08:06.4	887.8	0.024	2296.97
SN 2017hzw	17/11/13	23/07/30	5.7	02:05:18.13	53:12:13.4	226.9	0.030	188.55
SN 2018cqi	18/06/13	23/08/13	5.2	09:40:21.46	−06:59:19.8	91.4	0.036	36.58
SN 2018gkx	18/09/08	23/08/16	4.9	13:52:19.22	55:38:28.3	646.0	0.033	1656.56
SN 2019agi	19/01/25	23/08/25	4.6	16:22:43.99	24:01:09.7	268.7	0.059	514.83
SN 2019rvb	19/10/02	23/08/26	3.9	16:38:10.16	68:27:49.1	890.5	0.026	2506.00
SN 2020kre	20/05/21	23/08/20	3.3	13:10:29.87	−01:18:51.1	640.9	0.077	3773.75
SN 2020onv	20/07/11	23/08/27	3.1	23:16:46.02	−23:18:37.1	435.8	0.038	857.37
SN 2020qxz	20/08/08	23/08/16	3.0	18:04:00.23	74:00:50.3	442.7	0.030	704.35
SN 2020abfe	20/11/14	23/08/26	2.8	20:00:03.31	10:09:04.2	426.1	0.042	924.34
SN 2020aeur	20/12/22	23/08/13	2.6	09:26:20.39	01:52:43.9	226.9	0.037	227.01
SN 2020aekp	20/12/27	23/08/26	2.7	15:43:11.39	17:48:47.2	236.1	0.049	330.99
SN 2022erq	22/03/11	23/08/16	1.4	18:33:25.36	44:05:11.7	296.8	0.032	340.57
SN 2022esa	22/03/12	23/08/26	1.5	16:53:57.60	−09:42:10.3	100.2	1.129 ± 0.052*	1360.22 ± 62.65*
SN 2022esa	22/03/12	24/10/19	2.6	16:53:57.60	−09:42:10.3	100.2	0.799 ± 0.036*	962.30 ± 43.07*

NOTE—* Measurements represent peak flux density for SN 2022esa using CASA `imfit` (see Section 2 and 4)

be used to constrain the mass-loss rates of our Ia-CSM SN sample in Section 4, given their upper limits on their 6 GHz radio emission obtained in Section 2.

3.1. Synchrotron emission

We roughly follow the same synchrotron emission modeling procedure for Type Ia SNe that was used in previous papers (e.g. Chomiuk et al. 2012b, 2016; Harris et al. 2023; Hosseinzadeh et al. 2023), with a few modifications to the shock dynamics described in Section 3.2. We refer the reader to these papers for details of the model, but include a brief description here.

The model follows the classical Chevalier (1982) model of synchrotron emission from SN ejecta interacting with CSM. The density profile of the CSM is assumed to be wind-like, with $\rho = \dot{M}/4\pi r^2 v_{wind}$, where \dot{M} is the wind’s constant mass-loss rate, and v_{wind} is the wind velocity. Although idealized, a wind-like CSM is a reasonable approximation for single-degenerate progenitors with red-giant or AGB companions that are continuous mass-losing systems, and are considered strong candidates for our Ia-CSM SNe. Previous radio studies of SNe have often assumed a wind-like CSM since it provides convenient, self-similar solutions for shock dynamics and the resulting radio light curves, making it possi-

ble to explore vast parameter space of CSM properties (see examples in [Chevalier & Fransson 2017](#)). Finally, a CSM wind profile is generally the model assumed in optical studies of Ia-CSM SNe for estimation of mass-loss rates (see discussion in Section 5), so we assume the same for consistency with our radio-based results.

Broadly speaking, the optically-thin synchrotron luminosity depends on the volume of the shock, the energy density in the amplified magnetic field, and the energy density in relativistic electrons. This electron population is assumed to have a characteristic power-law spectrum, $N(E) = N_0 E^{-p}$, where we assume $p = 3$ that is commonly observed in Type Ib/c SNe ([Soderberg et al. 2005, 2006](#)) and is often assumed for Type Ia SNe ([Chomiuk et al. 2016](#)). The energy density in relativistic electrons is assumed to be $\propto \epsilon_e \rho v^2$, where ϵ_e is the fraction of the shock energy in the relativistic electrons, ρ is the density of CSM that the shock is interacting with at the time of radio observation, v is the shock velocity. The amplified magnetic field is assumed to scale with the shock energy as $B^2 \propto \epsilon_B \rho v^2$ ([Chomiuk & Wilcots 2009; Thompson et al. 2009](#)), where ϵ_B , analogous to ϵ_e , is the fraction of shock energy in the amplified magnetic field. The resulting optically-thin luminosity will have a frequency dependence $\propto \nu^{-1}$. At early times, we assume this emission will be suppressed by synchrotron self-absorption and free-free absorption by the dense CSM. For self-absorption, we use the form of the radio spectrum laid out in [Chevalier \(1998\)](#) that self-consistently accounts for a $L_\nu \propto \nu^{-2.5}$ turnover at lower frequencies, where the self-absorption optical depth > 1 . For free-free absorption, we multiply the luminosity by a factor $\epsilon^{-\tau_{\text{ff}}}$, where τ_{ff} is the free-free optical depth at a given wavelength (λ), which we derive from Equation (2.3) of [Fransson et al. \(1996\)](#) as:

$$\tau_{\text{ff}} \approx 0.46 \lambda^2 \left(\frac{\dot{M}_{-5}}{v_{\text{wind},10}} \right)^2 T_5^{-3/2} v_4^{-3} \left(\frac{t}{11.57 \text{d}} \right)^{-3} \quad (1)$$

where \dot{M}_{-5} is the mass loss rate in units of $10^{-5} M_\odot \text{ yr}^{-1}$, $v_{\text{wind},10}$ is the wind velocity in units of 10 km s^{-1} , T_5 is the wind temperature in 10^5 K (which we refer to as T_{wind}), and v_4 is the ejecta velocity in 10^4 km s^{-1} , and t is the time elapsed between SN explosion and the radio observation in question.

Our goal is to obtain constraints on the mass-loss rate given the observed radio luminosity (or upper limit) for each SN, but these constraints will depend on the values of several tunable parameters in our model. Based on [Harris et al. \(2023\)](#), the parameters expected to have the largest impact on the interpretation of the radio upper limits are ϵ_B , ϵ_e , and T_{wind} . As per convention, we assume the range of $\epsilon_B = 0.01 - 0.1$ ([Chomiuk et al.](#)

	Model A	Model B	Model C
ϵ_B	0.1	0.1	0.01
$T_{\text{wind}} \text{ (K)}$	10^5	2×10^4	2×10^4

Table 2. Parameter values of the different radio light curve models for wind-like CSM explored in this paper.

[2012b](#)), while keeping $\epsilon_e = 0.1$ for every model (see Section 5 for a discussion of these ranges). The values for T_{wind} are expected to vary between $2 \times 10^4 \text{ K}$ to 10^5 K for wind-like CSM around SNe ([Lundqvist et al. 2013](#)). In reality, both parameters will likely vary with time as the shock slows down and the post-shock conditions change, but for simplicity, we discuss our results for different constant values of T_{wind} and ϵ_B (Table 2) in order to provide an idea of the extent to which the various parameters affect the shape of the light curve, and therefore how they change the corresponding mass-loss rates.

For the remainder of this paper, we will be assuming $\mathbf{v}_{\text{wind}} = 100 \text{ km s}^{-1}$ and a frequency $\nu = 6 \text{ GHz}$ for the light curve calculations.

3.2. Shock radius and velocity

The evolution of the radio light curves depends on the shock dynamics (i.e., the radius and velocity). For this paper, we use the set of solutions from [Tang & Chevalier \(2017, hereafter, TC17\)](#) that describes the SN blast wave as it evolves from the ejecta-dominated (ED) phase to the Sedov-Taylor (ST) phase, in contrast with our previous papers (e.g., [Chomiuk et al. 2012b, Chomiuk et al. 2016](#), etc.) where we assume the SN shock is ED. The relevant CSM density range for SNe Ia-CSM can be much higher than normal SNe Ia, so the swept-up CSM can be comparable to or even exceed the ejecta mass within the timescales of our observations. For example, for $\dot{M} \approx 1.0 \times 10^{-2} M_\odot \text{ yr}^{-1}$ and $v_{\text{wind}} = 100 \text{ km s}^{-1}$, Equation 25 in [Tang & Chevalier \(2017\)](#) predicts that the swept-up mass will become dynamically important (i.e., $\geq M_{\text{ej}}$) as early as 7.9 yrs after explosion. At this and later times, the radius and velocity is expected to follow a ST solution, and the TC17 model accounts for this transition by smoothly connecting the ED phase to the ST phase. From these solutions, we are able to determine a shock radius and velocity for ejecta interacting with wind density profiles at late observation times.

For the steep ($n > 5$) ejecta profiles that are typically assumed for SNe, Eqs. (24) and (25) from [Tang & Chevalier \(2017\)](#) give:

$$R_b^*(t^*) = [(\zeta_b t^{*(n-3)/(n-s)})^{-\alpha} + (\xi t^{*2})^{-\alpha/(5-s)}]^{-1/\alpha}, \quad (2)$$

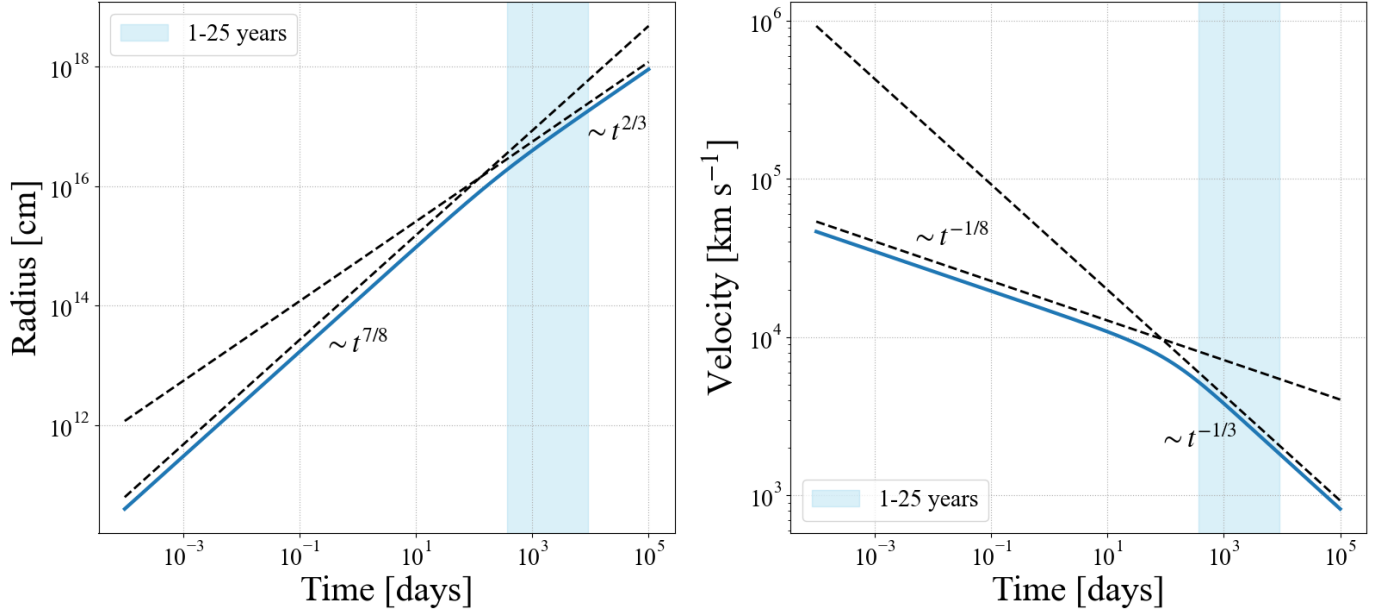


Figure 1. The time evolution of the forward shock radius (left panel) and velocity (right panel) from the TC17 model (Section 3.2) for the case of $E_{51} = 1.0$, $M_{ej} = 1.44 M_{\odot}$, and $\dot{M}/v_{wind} = 0.1 M_{\odot} \text{ yr}^{-1}$ (100 km s^{-1}) $^{-1}$. The vertical blue shaded section represents the time range at which our radio observations were obtained. Dashed lines represent the asymptotic solutions for the ejecta-dominated ($n = 10$ density profile) and Sedov-Taylor cases.

and

$$v_b^*(t^*) = \frac{dR_b^*}{dt^*}, \quad (3)$$

respectively. Here R_b^* , v_b^* and t^* are dimensionless radius, velocity and age, which are related to the physical radius (R_b), velocity (v_b) and age (t) of the shock as $R_b^* = R_b/R_{ch}$, $v_b^* = v_b/v_{ch}$ and $t^* = t/t_{ch}$, where “ X_{ch} ” denote the characteristic variables that are defined as:

$$R_{ch} = (12.9 \text{ pc}) M_{ej} \dot{M}_{-5}^{-1} v_{wind,10} \quad (4)$$

$$t_{ch} = (1772 \text{ yr}) E_{51}^{-1/2} M_{ej}^{3/2} \dot{M}_{-5}^{-1} v_{wind,10} \quad (5)$$

$$v_{ch} = (7118.39 \text{ km s}^{-1}) E_{51}^{1/2} M_{ej}^{-1/2}. \quad (6)$$

where M_{ej} is the ejecta mass in terms of M_{\odot} , and E_{51} is the kinetic energy in units of 10^{51} erg.

For a Type Ia-CSM SNe, we follow the model of an ejecta envelope with a steep density profile $n = 10$, and a wind density profile $s = 2$ (Harris et al. 2023). The values of the coefficients ζ_b , α , and ξ are drawn from Tables 4 and 6 of Tang & Chevalier (2017) for an $n = 10$ ejecta profile and wind-like ($s = 2$) CSM profile. The resulting solution for the dimensionless radius and velocity, after some algebraic re-arrangement, is

$$R_b^*(t^*) = 1.03t^{*(0.875)}[1 + 3.52t^{*(0.95)}]^{-0.219} \quad (7)$$

and

$$v_b^*(t^*) = 1.03t^{*(-0.125)}[1 + 2.79t^{*(0.95)}][1 + 3.52t^{*(0.95)}]^{-1.219}. \quad (8)$$

Throughout the paper, we will assume a standard SN Ia explosion with $M_{ej} = 1.44 M_{\odot}$ and $E_{51} = 1$.

Figure 1 illustrates the evolution of the shock radius and velocity from Eqs. (7) and (8). The radius follows the self-similar driven wave (SSDW) solution (Chevalier 1982; Nadezhin 1985), with $R \sim t^{7/8}$ at early times (i.e. the ejecta-dominated phase), and then approaches $R \sim t^{2/3}$ for late times (i.e. the Sedov-Taylor phase, following the self-similar Sedov-Taylor solution) (Taylor 1946; Sedov 1959). Since $v = dR/dt$, we see a trend of $v \sim t^{-1/8}$ in the ED phase, which then approaches $v \sim t^{-1/3}$ during the ST phase. The onset of the ST phase will occur earlier for denser CSM.

3.3. Basic Properties of Radio Light Curves

The radio light curves from the model described in the previous sub-sections are summarized in Figure 2. The shape of the light curves are similar to what has been seen in previous papers. At early times absorption processes dominate, but as the SN expands, the optical depths of the absorption processes decrease, and the emerging emission increases. Once the emission becomes optically thin, the light curves peak and then decline. This fading is primarily because both the energy

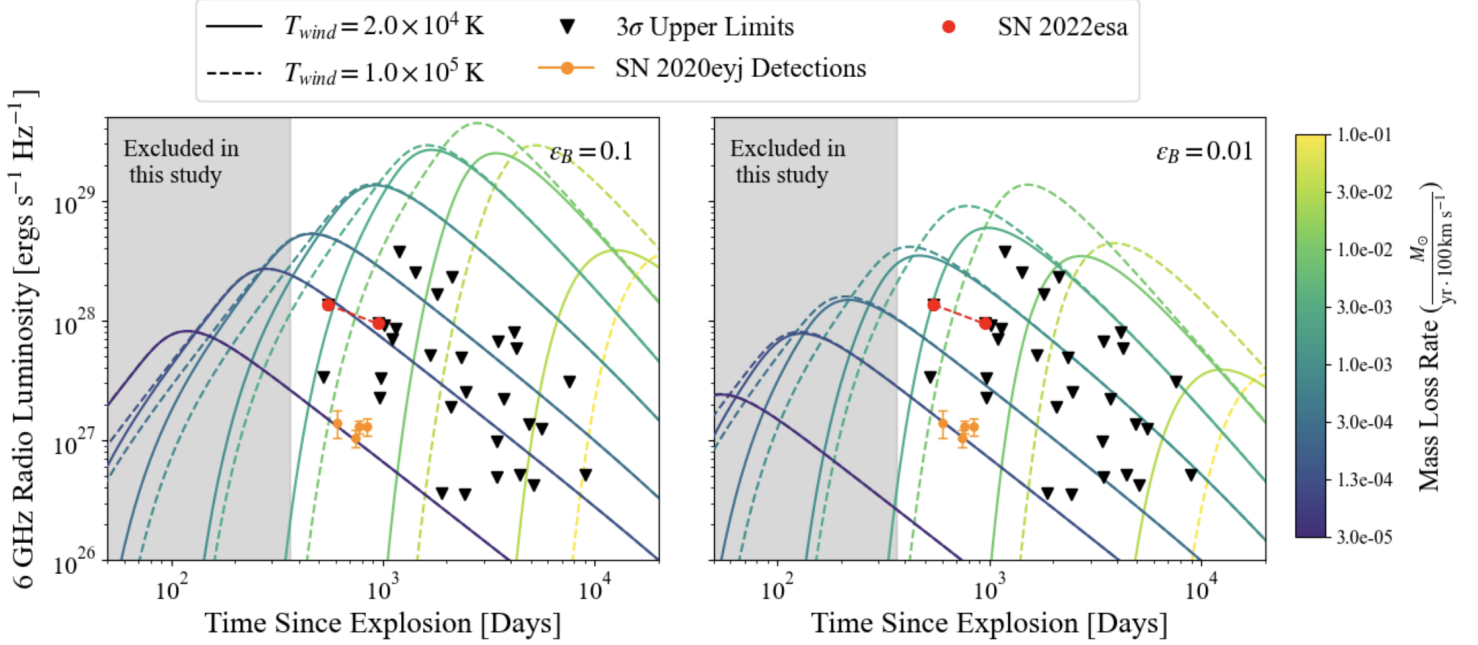


Figure 2. Predicted 6 GHz radio light curves for SNe Ia-CSM, shown alongside radio observations in this paper and from the literature. Solid curves correspond to the case of $T_{\text{wind}} = 2.0 \times 10^4$ K, and dashed curves for $T_{\text{wind}} = 10^5$ K. Left panel shows the case of $\epsilon_B = 0.1$, and the right panel shows $\epsilon_B = 0.01$ (both panels assume $\epsilon_e = 0.1$). Light curves span a range of \dot{M}/v_{wind} from $3 \times 10^{-5} M_{\odot} \text{ yr}^{-1}$ (dark blue lines) to $0.1 M_{\odot} \text{ yr}^{-1}$ (yellow lines), assuming $v_{\text{wind}} = 100 \text{ km s}^{-1}$. The shaded gray region represents SNe Ia < 1 yr, which are excluded in this study. SNe with 3σ upper limits are plotted as inverted black triangles. The radio detections of SN 2022esa from 2023 and 2024 are shown as red circles connected by a dashed line. Literature measurements of SN 2020eyj from Kool et al. (2023) and Yang et al. (2023) (scaled to 6 GHz) is shown as orange points. See Section 4 for more details.

in the electrons and the magnetic fields that are powering the emission are proportional to the shock energy ($\sim \rho v_s^2$). While the pre-shock density ρ decreases as r^{-2} , the shock also continues to decelerate as it loses energy to interaction with the surrounding, resulting in an overall decrease in synchrotron emission with time.

The different color lines in Figure 2 explore a sequence of \dot{M}/v_{wind} values. As the CSM becomes denser (i.e., higher \dot{M}/v_{wind}), the light curves become brighter due to the increasing reservoir of shock energy (ρv_s^2) available for the amplification of magnetic fields and relativistic electrons. The duration of the free-free absorbed phase of the light curve is also longer for denser CSM (see Eq 1), leading to the light curves peaking later in time. This is why early-time radio observations would have missed detection of SNe with denser CSM. Above a certain mass-loss rate however ($\gtrsim 5 \times 10^{-3} M_{\odot} \text{ yr}^{-1}$), the light curves begin to become fainter. This is primarily because at this point, the onset of the ST phase occurs *before* the light curve becomes optically-thin (i.e. $\tau_{\text{ff}} = 1$). The light curve in the ST phase declines faster because of the faster deceleration of the shock ($v \sim t^{-1/3}$). On top of this, the age at which the light curve peaks is delayed during the ST phase as the shock

is evolving slower, which delays the age at which $\tau_{\text{ff}} = 1$ (Eq. 1). The combination of these effects produces light curves that peak and then decline at fainter luminosities for higher mass-loss rates. This contrasts with the behavior of light curves evolving with an ED-only solution, and this is discussed further in Appendix A.

Figure 2 also illustrates the impact of the parameters ϵ_B and T_{wind} . Lower ϵ_B means a smaller fraction of ρv^2 amplifies the magnetic fields, resulting in weaker fields, and thus fainter luminosities. We note that the parameter ϵ_e , which we hold constant in this paper but can be uncertain, will have a similar magnitude of effect on the light curves as ϵ_B . The T_{wind} parameter affects the free-free optical depth $\tau_{\text{ff}} \sim T_{\text{wind}}^{-3/2}$ as seen in Eq. (1), so hotter CSM is less opaque to synchrotron emission. We therefore see the light curves for the hotter CSM (dashed lines in Figure 2) become optically thin at earlier times. The difference between the $T_{\text{wind}} = 1 \times 10^5$ K and 2×10^4 K becomes more dramatic at higher mass-loss rates, because of the effect of the ST phase described above.

3.4. Measuring mass-loss rates with the light curves

We apply the light curve model described in Section 3.1 to the observed luminosities (or upper limits) from Table 1 to constrain the possible values of \dot{M}/v_{wind} for each SN, using the different parameter combinations described in Table 2. In the case of a detection, we simply check for what value of \dot{M}/v_{wind} threads the light curve through the data point(s). For non-detections, which represent the majority of our sample, we can constrain the range of mass-loss rates ruled out by the luminosity limit as illustrated in Figure 3. At the given age of the SN, there will be a range of mass-loss rates for which the resulting luminosities at that age exceed the 3σ upper limit. These are the shaded regions in Figure 3, and represent the range of \dot{M}/v_{wind} that can be ruled out. The lower bound of this range comes from the optically-thin (decreasing) part of the light curves, while the upper bound comes from the optically-thick (rising) parts (this idea is better illustrated through the comparison of the variance in the optically-thick portion of the light curves in the leftmost panel of Figure 2 to the upper limits derived for Models A and B in Table 3). The range will additionally depend on the assumed values of ϵ_B and T_{wind} , and we discuss this further in Section 4.

Figure 3 also nicely illustrates the benefit of obtaining late-time observations for our sample. For the same upper limit, observations at 30 days would have only ruled out an order-of-magnitude range of possible mass-loss rates, while at 10 years, more than a two orders-of-magnitude range is ruled out, shifted to the *higher* values of \dot{M}/v_{wind} that are more relevant for SNe Ia-CSM. This is again due to the free-free absorption described in the previous section, which suppresses the radio emission from SNe for longer periods at higher mass-loss rates.

4. RESULTS

Most of the SNe (28 out of 29) in our sample are non-detections at 6 GHz, and their 3σ upper limits are shown in Figure 2. Based on the synchrotron emission model in Section 3, these upper limits rule out a range of mass-loss rates for each SN, shown in Figure 4, with the specific ranges for each SN reported in Table 3.

We find that the radio upper limits rule out the mass-loss rate range between $\sim 10^{-4} - 10^{-2} \text{ M}_{\odot} \text{ yr}^{-1}$ (assuming $v_w = 100 \text{ km s}^{-1}$) for most of our sample, with the exact ruled-out range varying with the SN age when the radio observation was carried out, as well as the assumed values of ϵ_B and T_{wind} . For example, decreasing ϵ_B by 1 dex (i.e. from 0.1 to 0.01) yields an increase of 0.68 dex in the \dot{M} lower limits and a decrease of 0.05 dex in the upper limits, on average. The varia-

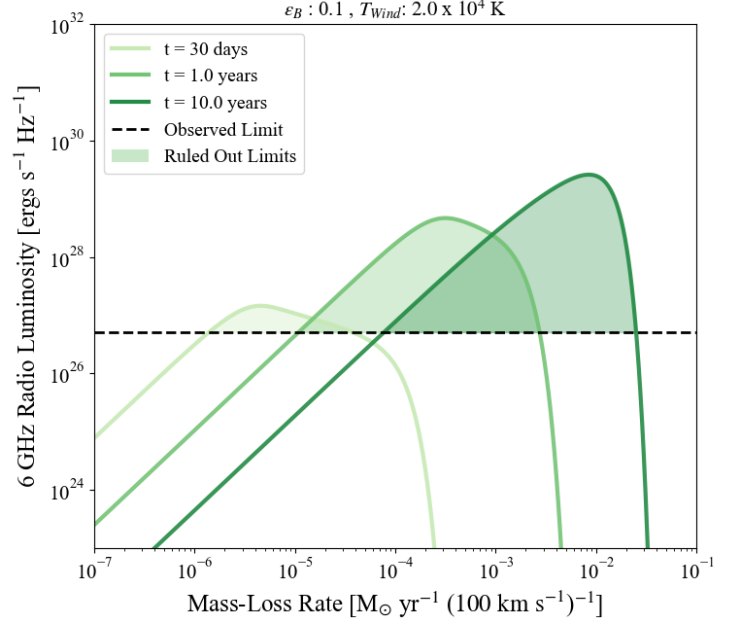


Figure 3. Illustration of how we use radio upper limits to constrain the range of *ruled-out* mass-loss rates \dot{M}/v_{wind} (green shade). Each light curve (green solid) shows the predicted luminosity for different mass-loss rates at a given SN age (30 days, 1 year, 10 years). The range of mass-loss rates where the predicted luminosity exceeds the measured upper limit (dashed line) are ruled out. Due to the light curve shape for wind-like CSM, later-time observations are more effective at ruling out a greater (and higher) range of mass-loss rates.

tion of T_{wind} has more of an effect on the upper limits of \dot{M} , while there is a negligible effect on the lower limits when retaining the same value for ϵ_B . For instance, when $\epsilon_B = 0.1$ stays the same and T_{wind} increases by 0.7 dex (from $2.0 \times 10^4 \text{ K}$ to $1.0 \times 10^5 \text{ K}$), the change in the lower limit is negligible while the upper limits increase by an average of 0.35 dex. Lowering the value of ϵ_B for the same T_{wind} pushes down the light curve to fainter luminosities, which makes the lower limit of the ruled-out mass-loss rates less constraining.

The range of excluded mass-loss rates progressively shifts higher for older SNe in Figure 4. For instance, we see that our radio observations of SN 2022erq rule out $2.0 \times 10^{-4} < \dot{M} < 3.7 \times 10^{-3} \text{ M}_{\odot} \text{ yr}^{-1}$, for $\epsilon_B = 0.01$, $T_{\text{wind}} = 2 \times 10^4 \text{ K}$, and $v_{\text{wind}} = 100 \text{ km s}^{-1}$, whereas we exclude $8.7 \times 10^{-4} < \dot{M} < 3.8 \times 10^{-2} \text{ M}_{\odot} \text{ yr}^{-1}$ for SN 1999E for the same values of ϵ_B , T_{wind} , and v_{wind} (exact values are recorded in Table 3). This is because of the effect observed in Figure 3 and discussed in Section 3.4, where at older ages, the SN observations are more sensitive to emission from higher mass-loss rates that emerge progressively later in time. The progression in Figure 6 is however non-monotonic, as some SNe are

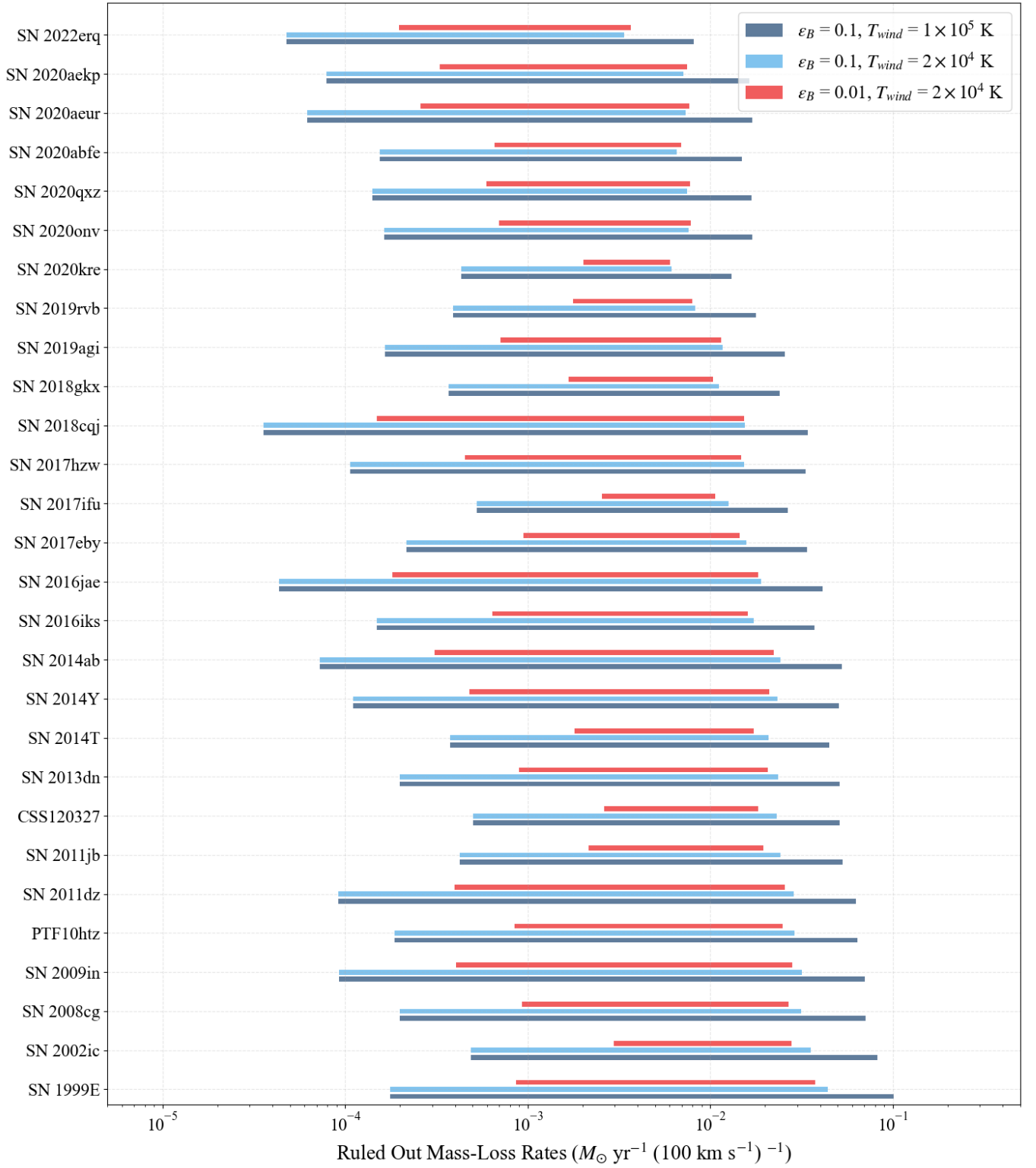


Figure 4. The range of mass-loss rates ruled out by the radio upper limits for each SN. For each SN, we show ranges for the three models in Table 2 for the parameters ϵ_B and T_{wind} . See Section 4 for details.

Table 3. The range of ruled-out mass-loss rates for our Ia-CSM SNe computed with the [Tang & Chevalier \(2017\)](#) model. For each model from Table 2, we note the lower and upper limit of the ruled out range in $M_{\odot} \text{ yr}^{-1}$ (100 km s^{-1}) $^{-1}$. These ranges are shown visually for each SN in Figure 4.

SN	Model A	Model B	Model C
SN 1999E	$1.8 \times 10^{-4} - 1.0 \times 10^{-1}$	$1.8 \times 10^{-4} - 4.4 \times 10^{-2}$	$8.7 \times 10^{-4} - 3.8 \times 10^{-2}$
SN 2002ic	$4.9 \times 10^{-4} - 8.2 \times 10^{-2}$	$4.9 \times 10^{-4} - 3.6 \times 10^{-2}$	$3.0 \times 10^{-3} - 2.8 \times 10^{-2}$
SN 2008cg	$2.0 \times 10^{-4} - 7.1 \times 10^{-2}$	$2.0 \times 10^{-4} - 3.2 \times 10^{-2}$	$9.4 \times 10^{-4} - 2.7 \times 10^{-2}$
SN 2009in	$9.3 \times 10^{-5} - 7.0 \times 10^{-2}$	$9.3 \times 10^{-5} - 3.2 \times 10^{-2}$	$4.1 \times 10^{-4} - 2.8 \times 10^{-2}$
PTF10htz	$1.9 \times 10^{-4} - 6.4 \times 10^{-2}$	$1.9 \times 10^{-4} - 2.9 \times 10^{-2}$	$8.5 \times 10^{-4} - 2.5 \times 10^{-2}$
SN 2011dz	$9.2 \times 10^{-5} - 6.3 \times 10^{-2}$	$9.2 \times 10^{-5} - 2.9 \times 10^{-2}$	$4.0 \times 10^{-4} - 2.6 \times 10^{-2}$
SN 2011jb	$4.2 \times 10^{-4} - 5.3 \times 10^{-2}$	$4.2 \times 10^{-4} - 2.4 \times 10^{-2}$	$2.2 \times 10^{-3} - 2.0 \times 10^{-2}$
CSS120327	$5.0 \times 10^{-4} - 5.1 \times 10^{-2}$	$5.0 \times 10^{-4} - 2.3 \times 10^{-2}$	$2.6 \times 10^{-3} - 1.8 \times 10^{-2}$
SN 2013dn	$2.0 \times 10^{-4} - 5.1 \times 10^{-2}$	$2.0 \times 10^{-4} - 2.4 \times 10^{-2}$	$9.0 \times 10^{-4} - 2.1 \times 10^{-2}$
SN 2014T	$3.8 \times 10^{-4} - 4.5 \times 10^{-2}$	$3.8 \times 10^{-4} - 2.1 \times 10^{-2}$	$1.8 \times 10^{-3} - 1.7 \times 10^{-2}$
SN 2014Y	$1.1 \times 10^{-4} - 5.1 \times 10^{-2}$	$1.1 \times 10^{-4} - 2.3 \times 10^{-2}$	$4.8 \times 10^{-4} - 2.1 \times 10^{-2}$
SN 2014ab	$7.2 \times 10^{-5} - 5.3 \times 10^{-2}$	$7.2 \times 10^{-5} - 2.4 \times 10^{-2}$	$3.1 \times 10^{-4} - 2.2 \times 10^{-2}$
SN 2016iks	$1.5 \times 10^{-4} - 3.7 \times 10^{-2}$	$1.5 \times 10^{-4} - 1.7 \times 10^{-2}$	$6.4 \times 10^{-4} - 1.6 \times 10^{-2}$
SN 2016jae	$4.4 \times 10^{-5} - 4.1 \times 10^{-2}$	$4.4 \times 10^{-5} - 1.9 \times 10^{-2}$	$1.8 \times 10^{-4} - 1.8 \times 10^{-2}$
SN 2017eby	$2.2 \times 10^{-4} - 3.4 \times 10^{-2}$	$2.2 \times 10^{-4} - 1.6 \times 10^{-2}$	$9.5 \times 10^{-4} - 1.5 \times 10^{-2}$
SN 2017ifu	$5.3 \times 10^{-4} - 2.7 \times 10^{-2}$	$5.3 \times 10^{-4} - 1.3 \times 10^{-2}$	$2.6 \times 10^{-3} - 1.1 \times 10^{-2}$
SN 2017hzw	$1.1 \times 10^{-4} - 3.3 \times 10^{-2}$	$1.1 \times 10^{-4} - 1.5 \times 10^{-2}$	$4.6 \times 10^{-4} - 1.5 \times 10^{-2}$
SN 2018cqi	$3.6 \times 10^{-5} - 3.4 \times 10^{-2}$	$3.6 \times 10^{-5} - 1.6 \times 10^{-2}$	$1.5 \times 10^{-4} - 1.5 \times 10^{-2}$
SN 2018glx	$3.7 \times 10^{-4} - 2.4 \times 10^{-2}$	$3.7 \times 10^{-4} - 1.1 \times 10^{-2}$	$1.7 \times 10^{-3} - 1.0 \times 10^{-2}$
SN 2019agi	$1.7 \times 10^{-4} - 2.6 \times 10^{-2}$	$1.7 \times 10^{-4} - 1.2 \times 10^{-2}$	$7.1 \times 10^{-4} - 1.2 \times 10^{-2}$
SN 2019rvb	$3.9 \times 10^{-4} - 1.8 \times 10^{-2}$	$3.9 \times 10^{-4} - 8.3 \times 10^{-3}$	$1.8 \times 10^{-3} - 8.0 \times 10^{-3}$
SN 2020kre	$4.3 \times 10^{-4} - 1.3 \times 10^{-2}$	$4.3 \times 10^{-4} - 6.2 \times 10^{-3}$	$2.0 \times 10^{-3} - 6.0 \times 10^{-3}$
SN 2020onv	$1.6 \times 10^{-4} - 1.7 \times 10^{-2}$	$1.6 \times 10^{-4} - 7.6 \times 10^{-3}$	$7.0 \times 10^{-4} - 7.9 \times 10^{-3}$
SN 2020qxz	$1.4 \times 10^{-4} - 1.7 \times 10^{-2}$	$1.4 \times 10^{-4} - 7.5 \times 10^{-3}$	$5.9 \times 10^{-4} - 7.8 \times 10^{-3}$
SN 2020abfe	$1.6 \times 10^{-4} - 1.5 \times 10^{-2}$	$1.6 \times 10^{-4} - 6.6 \times 10^{-3}$	$6.6 \times 10^{-4} - 6.9 \times 10^{-3}$
SN 2020aeur	$6.2 \times 10^{-5} - 1.7 \times 10^{-2}$	$6.2 \times 10^{-5} - 7.3 \times 10^{-3}$	$2.6 \times 10^{-4} - 7.7 \times 10^{-3}$
SN 2020aekp	$7.9 \times 10^{-5} - 1.6 \times 10^{-2}$	$7.9 \times 10^{-5} - 7.1 \times 10^{-3}$	$3.3 \times 10^{-4} - 7.5 \times 10^{-3}$
SN 2022erq	$4.8 \times 10^{-5} - 8.1 \times 10^{-3}$	$4.8 \times 10^{-5} - 3.4 \times 10^{-3}$	$2.0 \times 10^{-4} - 3.7 \times 10^{-3}$

more distant than others, thus having shallower limits (e.g. the ruled out range of SN 2019agi is significantly smaller than the range for SN 2018cqj, even though they are a year apart, because SN 2018cqj is nearly three times closer).

We briefly discuss SN 2022esa, the only SN radio-detected SN in our sample. While it was initially classified as a SN Ia-CSM², re-inspection of the public TNS spectrum shows that the narrow lines are likely from the host galaxy, given the visible [O III] and [S II] lines in addition to the narrow Balmer lines. Removing these lines using SNID `emclip` (Blondin & Tonry 2007) does not provide a very reliable classification. In addition, a subsequent spectrum obtained at the Nordic Optical Telescope on 2022-07-17 show better matches with a stripped envelope core collapse supernova (Type Ib/c), and late nebular spectra reveal lines of oxygen and carbon but no lines from iron-peak elements (Yu-Jing Qin, private communication) which further argues for a core-collapse origin (Qin et al. in prep). A more detailed investigation of the object will be presented in Qin et al. in prep, but here we briefly note the radio evolution observed for 2022esa. Figure 5 shows the observed VLA measurements, showing a clear decline in radio emission similar to SN2020eyj, except that it is much brighter. The slope of the decline is slightly shallower than our Sedov-phase light curves. The mass-loss rates that best-fit these data-points are in the range of $(1.2 - 1.5) \times 10^{-4} M_{\odot} \text{ yr}^{-1}$ ($\epsilon_B = 0.1$) or $(5 - 6.4) \times 10^{-4} M_{\odot} \text{ yr}^{-1}$ ($\epsilon_B = 0.01$).

We also re-interpret the radio data for SN 2020eyj, which is still the only radio-detected Ia-CSM so far, with the modified radio light curve model in this paper. SN 2020eyj was observed at 5.1 GHz with e-MERLIN in Kool et al. (2023) on November 19th, 2021 then again during six consecutive days between April 6-12 of 2022. This SN was also observed with the VLA in Yang et al. (2023) on both April 14th and June 26th of 2022 (the data collected from these e-MERLIN and VLA observations are shown as orange points in Figure 2). SN 2020eyj was consistent with constant or slightly decreasing flux over these radio observations, meaning we can assume the emission is optically thin. We scale the e-MERLIN measurements to 6 GHz assuming the luminosity $L_{\nu} \propto \nu^{-1}$. We find that the luminosities are consistent with mass-loss rates of $3.4 \times 10^{-5} M_{\odot} \text{ yr}^{-1}$ for $\epsilon_B = 0.1$ and $1.4 \times 10^{-4} M_{\odot} \text{ yr}^{-1}$ for $\epsilon_B = 0.01$. The assumed value of T_{wind} should not affect the mass-loss rates, as the emission is optically-thin. Our measure-

ments are lower than in Kool et al. (2023) because of their lower fitted values of ϵ_B , which we return to in Section 5.

5. DISCUSSION

Our results indicate that the majority of SNe Ia-CSM will likely not produce radio emission at 6 GHz on ~ 1 -25 yr timescales, at least with flux densities brighter than $\sim 35 \mu\text{Jy}$, in contrast with SN 2020eyj³. The non-detections of our sample also stand in contrast with Type IIn SNe, the core-collapse cousins of SNe Ia-CSM, where at least 10% of the population with radio observations have detectable light curves that peak on timescales of about 2–34 years (substantially longer than other core-collapse SN subtypes) at luminosities comparable to our upper limits (see Chandra 2018; Bietenholz et al. 2021, and references therein). One possibility is that, assuming both types of SNe explode with the canonical 10^{51} erg energy, the Ia-CSM SNe on average have lower CSM densities than Type IIn SNe, and thus the radio-detectable Ia-CSM population may be peaking at times similar to 2020eyj, i.e. a year or two after explosion (as opposed to longer few-decade timescales like Type IIn). A similar reasoning was applied to X-ray observations of SNe Ia-CSM, where the reason why SN 2012ca still remains the only X-ray visible SN Ia is because it was likely observed at an opportune moment, when the ambient medium was dense enough to produce visible X-ray but not too dense to suffer complete absorption (Bochenek et al. 2018; Dwarkadas 2023, 2024). We only have two SNe with radio observations at $\lesssim 2$ yr ages – SN 2022erq which was a non-detection, and SN 2022esa, which was likely a peculiar Ic. Following up a larger sample of SNe Ia-CSM on these 1-2 year timescales in future will help test this hypothesis.

The range of mass-loss rates ruled out by our radio survey, roughly between $10^{-4} - 10^{-2} M_{\odot} \text{ yr}^{-1}$, are somewhat in tension with the mass-loss rates derived from optical observations of SNe Ia-CSM. These rates are most commonly been derived by modeling the broad component of the H α line as $L_{H\alpha} \propto \epsilon_{H\alpha} (\dot{M}/v_{wind}) v_s^3$, assuming the hydrogen in a spherically-symmetric CSM with r^{-2} profile is being collisionally excited by the shock (e.g. Chugai 1991; Salamanca et al. 1998). The observed luminosities and velocities of $\sim \text{few} \times 10^3 \text{ km s}^{-1}$, measured from the broad H α line profiles, yield mass-loss rates typically in the range of $10^{-4} - 10^{-2} M_{\odot} \text{ yr}^{-1}$, assuming $(100 \text{ km s}^{-1})^{-1}$ winds, and an efficiency $\epsilon_{H\alpha} = 0.1$ (e.g. Aldering et al. 2006; Silverman et al.

² TNS classification

³ We also note that 2020eyj was a He-rich Ia-CSM (Kool et al. 2023), which contrasts with our sample that are H-rich Ia-CSM.

2013; Sharma et al. 2023). These ranges of mass-loss rates are generally inconsistent with our radio-derived constraints on \dot{M} in Figure 4 for the same CSM geometry. Based on the radio measurements alone, the required mass-loss rates would have to be lower than $10^{-4} \text{ M}_{\odot} \text{ yr}^{-1}$ or higher than $10^{-2} - 10^{-1} \text{ M}_{\odot} \text{ yr}^{-1}$. Regarding the former possibility, we note that non-detections from earlier-time ($<1 \text{ yr}$) radio observations of Ia-CSM pushes the lower end of the ruled-out mass-loss rate range further down to $\lesssim 10^{-5.5} \text{ M}_{\odot} \text{ yr}^{-1}$ (100 km s^{-1}) $^{-1}$ (e.g. Dilday et al. 2012; Chomiuk et al. 2016). While such low mass-loss rates are more consistent with realistic progenitors like symbiotic binaries (Seaquist & Taylor 1990; Chomiuk et al. 2012b), they may under-predict the $\text{H}\alpha$ luminosities, requiring a substantially more efficient $\epsilon_{\text{H}\alpha}$ or faster shock velocities than measured from the broadened $\text{H}\alpha$.

Mass-loss rates higher than $0.1 \text{ M}_{\odot} \text{ yr}^{-1}$ (100 km s^{-1}) $^{-1}$ is also technically allowed by the radio limits, and we do note that mass-loss rates derived from modeling the bolometric light curves of Ia-CSM in Silverman et al. (2013) are $\gtrsim 10^{-1} \text{ M}_{\odot} \text{ yr}^{-1}$. These values however become significantly more inconsistent with wind-like CSM in single-degenerate systems. In fact, such copious winds are extreme even for typical supergiant stars, and only observed in luminous blue variable eruptions (Smith 2014). A possible way to reconcile the above tension between radio and optical observations is if, e.g., the CSM is not a wind, but rather discrete, dense shells produced by episodic mass-loss events such as common envelope ejections (e.g. common-envelope ejections, Livio & Riess 2003) or swept-up nova-shells (e.g. Wood-Vasey & Sokoloski 2006; Moore & Bildsten 2012). Such shell-like geometries, with thicknesses of up to four times the inner radii, have been proposed in some SNe Ia showing delayed interactions, like PTF11kx and SN 2002ic (e.g. Dilday et al. 2012; Graham et al. 2017; Harris et al. 2018). This shock+shell interaction beginning at a few months would illuminate in $\text{H}\alpha$, but then rapidly diminish once the shock crosses over the shell, eluding later radio observations. In fact, radio observations of SN 2020ej were reproduced with a best-fit shell $\sim 0.3 \text{ M}_{\odot}$ located within 10^{16} cm , but the resulting luminosity is expected to diminish well below $10^{27} \text{ erg s}^{-1} \text{ Hz}^{-1}$ (the lower end of our limits in Figure 2) by 10^3 days according to Figure 4 in Kool et al. (2023). Modeling such discontinuous or shell-like CSM (e.g. with the formalism of Harris et al. 2016, 2021) will be attempted in future papers, and will benefit from coordinated optical and radio observations to correctly constrain the extents of the shells.

Another possible way of addressing the tension is if our microparameters (ϵ_B and ϵ_e) are significantly lower than the range assumed here ($10^{-2} - 10^{-1}$). Lowering these parameters makes the radio luminosities fainter (as discussed in Section 3.3), which shrinks the range of ruled-out mass-loss rates further (Figure 4). For $\epsilon_B < 10^{-4}$, the light curves for the majority of our sample fall below our observed limits, and no mass-loss rate can be ruled out. Kool et al. (2023) showed that the bolometric light curve of SN 2020ej suggested wind mass-loss rates of 10^{-4} to $3 \times 10^{-3} \text{ M}_{\odot} \text{ yr}^{-1}$ for $v_{\text{wind}} = 100 \text{ km s}^{-1}$, which could fit the radio observations only if $\epsilon_B = 1.7 \times 10^{-3}$ or 1.5×10^{-5} . On the other hand, $\epsilon_B = 0.1$ was consistent with the radio light curve of SN 2020ej for a shell-like CSM geometry like in Harris et al. (2016) (Figure 4 in Kool et al. 2023). Unfortunately, the observational and theoretical basis for determining values of ϵ_e and ϵ_B is still a topic of debate. Values of $\epsilon_B = 0.01 - 0.1$ have been inferred in relativistic SNe (e.g. Chevalier & Fransson 2006; Soderberg et al. 2012), and given the similar polytropic structure of their progenitors and white dwarfs, this range has been conventionally assumed for SNe Ia (Chomiuk et al. 2012b). Values of ϵ_e and $\epsilon_B \gtrsim 10^{-3}$ have been inferred in shocks with velocities of a few $\times 10^3 \text{ km s}^{-1}$ in the Kepler SN remnant (Reynolds et al. 2021), also a candidate for a Type Ia that exploded in a dense CSM (e.g., Katsuda et al. 2015). Similarly low values were also derived from radio light curves of some Type II SNe (Chevalier et al. 2006). Theoretically, a clear prescription of how these parameters change with the shock conditions and shock structure in collisionless shocks is also yet to be established (see review in Marcowith et al. 2016), so we do not have firm evidence leading us to prefer lower values of ϵ_B .

6. CONCLUSIONS

Motivated by the recent (and first ever) radio detection of SN Ia-CSM SN 2020ej at $\sim 1.5 - 2 \text{ yrs}$, we have carried out the largest late-time ($>1 \text{ yr}$) radio survey of SNe Ia-CSM to date. The goal was to detect synchrotron emission from shock interaction with a high-density CSM, as suggested by optical observations, that would have eluded earlier observations due to heavy synchrotron and free-free absorption.

We observed 29 historical SNe Ia-CSM with ages of 1–25 yrs with the Very Large Array for about 10–20 mins each, deep enough to detect emission at levels similar to SN 2020ej. Images were calibrated and reconstructed with standard pipelines, and the flux densities (or upper limits) at the SN locations were analyzed with standard synchrotron emission models from SN shocks interact-

ing with r^{-2} -like CSM wind. We used a new model of the shock dynamics from Tang & Chevalier (2017) that includes a Sedov-Taylor evolution of the shock if the swept-up CSM mass becomes comparable to or exceeds the ejecta mass. The new light curve model predicts increasingly fainter emission at higher mass-loss rates as a result of the enhanced deceleration of the forward shock.

Most of our SNe (28 out of 29) are radio non-detections down to 3σ limits of $\sim 35 \mu\text{Jy}$, implying that emergent radio emission (similar to SN 2020ejj) at these brightness levels on 1.5 – 25 yr timescales is unlikely in SNe Ia-CSM. The only radio-detected object in the sample, SN 2022esa, is most likely a peculiar SN Ic based on inspection of spectra taken at later epochs. Nevertheless, we have compiled the *largest* sample of SNe Ia-CSM with radio upper limits in this paper, which allows us for the first time to independently verify the mass-loss rates of SNe Ia-CSM quoted from optical observations. We find that the radio upper limits of our sample rule out mass-loss rates between $\sim 10^{-4}$ and $10^{-2} M_{\odot} \text{ yr}^{-1}$ (100 km s^{-1}) $^{-1}$ (though the range differs for each SN and assumed model parameter). This is inconsistent with the mass-loss rates predicted by models of the H α line, yet consistent with the high mass-loss rates ($> 10^{-1} M_{\odot} \text{ yr}^{-1}$) derived from bolometric light curve models of SNe Ia-CSM. We believe the best reasons are either that the CSM has more complex, discontinuous geometries than a wind (e.g. a shell that only produces a transient H α emission), or that the CSM can be a wind, but the efficiency parameters of accelerating electrons (ϵ_e) and amplifying magnetic fields (ϵ_B) in our model

are much smaller for SNe Ia-CSM ($< 10^{-4} - 10^{-3}$) than generally assumed for SNe Ia.

We hope the dataset presented here will be a valuable resource to the community for additional investigations of SNe Ia-CSM. We particularly encourage coordinated optical and radio observations to better constrain CSM with discontinuous, shell-like geometries. The upcoming Rubin observatory, as well as high-sensitivity all-sky radio surveys with DSA-2000 (Hallinan et al. 2019), SKA (Dewdney et al. 2009) and ngVLA (Murphy et al. 2018) will not only enable such coordinated observations, but also reach greater sensitivities than our current observations.

ACKNOWLEDGMENTS

O.G., G.S., C.E.H., and L.C. are grateful for support from NSF grants AST-2107070 and AST-2205628. M.P.T. acknowledges financial support through the Severo Ochoa grant CEX2021-001131-S and the Spanish National grant PID2023-147883NB-C21, funded by MCIU/AEI/ 10.13039/501100011033, as well as support through ERDF/EU. The National Radio Astronomy Observatory is a facility of the National Science Foundation operated under cooperative agreement by Associated Universities, Inc.

Facilities: VLA

Software: CASA (McMullin et al. 2007), astropy (Astropy Collaboration et al. 2022), matplotlib (Hunter 2007), scipy (Virtanen et al. 2020), numpy (Harris et al. 2020), photutils (Bradley et al. 2023).

APPENDIX

A. COMPARISON OF TANG & CHEVALIER (2017) WITH PREVIOUS MODELS

Here we discuss the difference between the light curves based on the shock dynamics of TC17 model that includes both ejecta-dominated and Sedov-Taylor evolution, and those assumed in previous radio studies of SNe Ia (e.g. Chomiuk et al. 2016) that only included the ejecta-dominated solution, $R \sim t^{(n-3)/(n-s)}$. For our assumed $n = 10$ ejecta and wind-like CSM ($s = 2$), the ejecta-dominated solution implies $R \sim t^{7/8}$ and $v \sim t^{-1/8}$. While the ejecta-dominated solution is applicable to the general SN Ia population where CSM densities are expected to be low (Chomiuk et al. 2016), it can lead to very different light curves at high CSM densities, compared to those including the Sedov Taylor phase.

This effect is illustrated in Figure 5, where we plot the ejecta-dominated+Sedov based light curve (the “TC17 model”) in solid, and the ejecta-dominated-only light curves from previous models (“Old Model”) in dashed. For lower mass loss rates ($< 10^{-4} M_{\odot} \text{ yr}^{-1}$), the light curves for the two models are almost identical since the shock is ejecta-dominated in both models; the Sedov phase has not set in during the timescale of our observations. At higher mass-loss rates, the difference between the two models become more dramatic, with the TC17 model showing decreasing luminosities with increasing mass-loss rate, while the old models show increasing luminosities. The difference as mentioned in Section

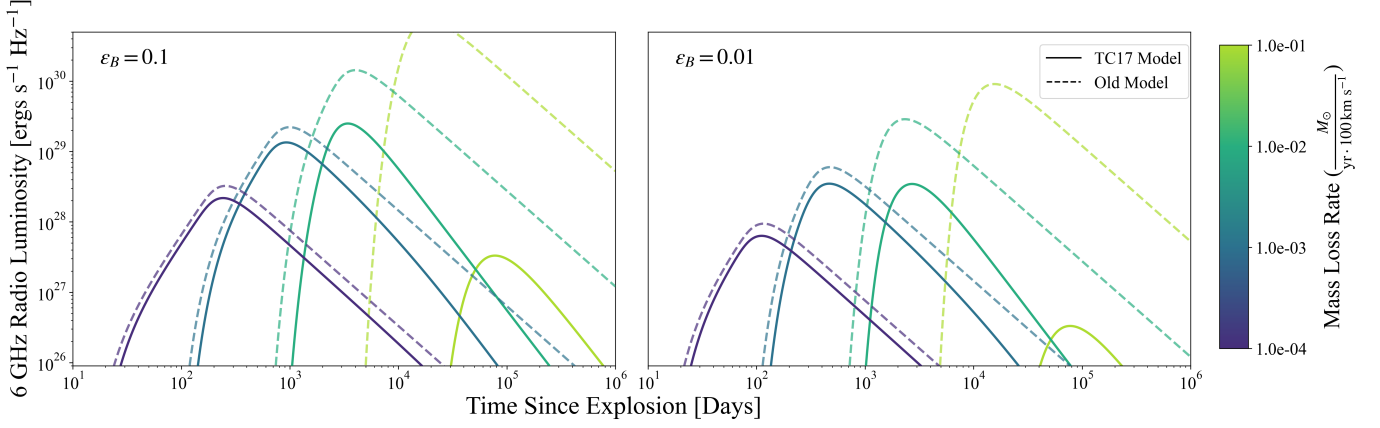


Figure 5. Comparison of light curves produced by different models. The solid lines make use of the dynamics from TC17, while the dashed lines represent the models of [Chomiuk et al. \(2016\)](#), which do not include the transition to the ST phase. The left panel shows models for $\epsilon_B = 0.1$, and the right panel for $\epsilon_B = 0.01$. Different color lines represent different values of \dot{M}/v_{wind} , according to the color bar at right.

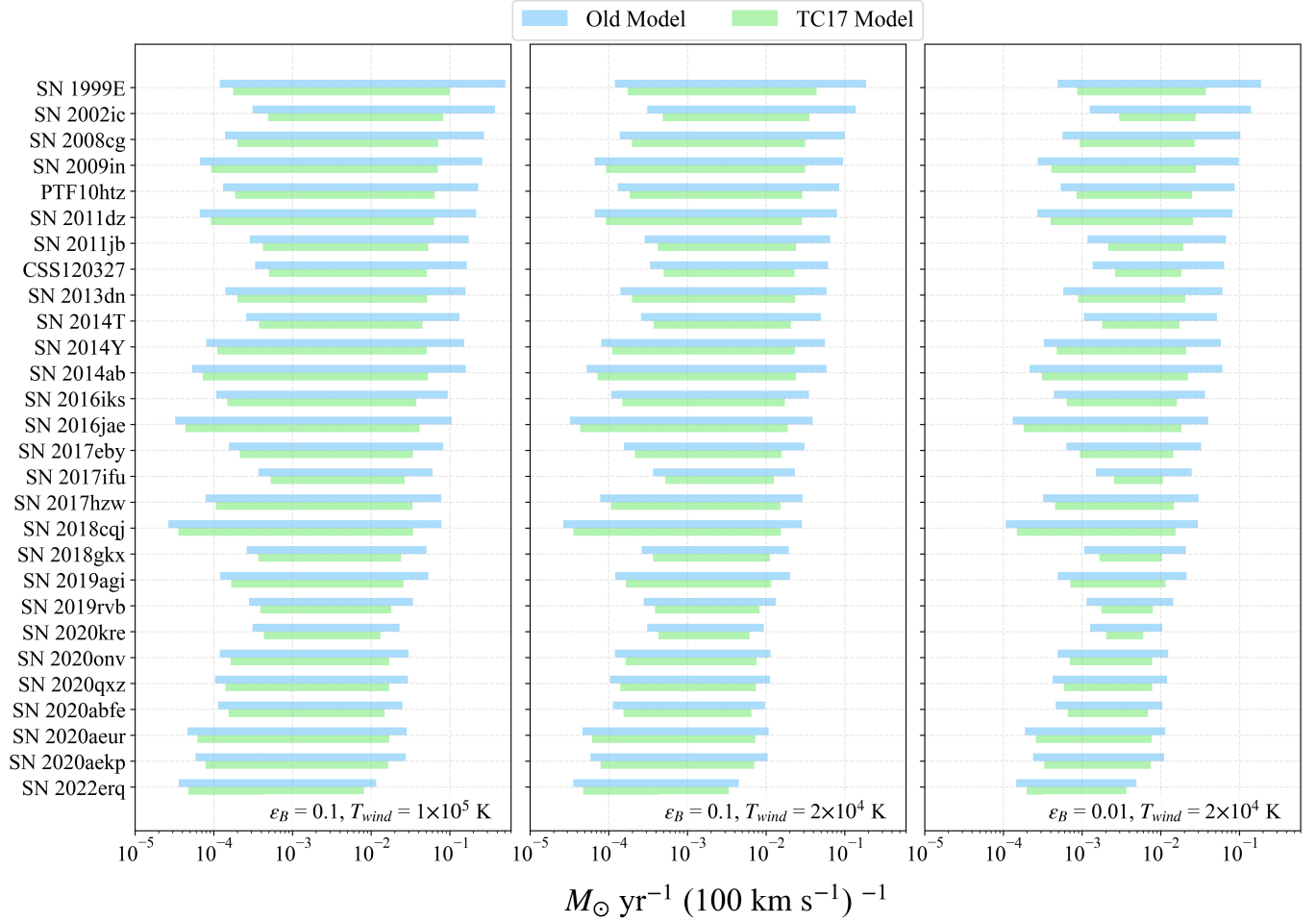


Figure 6. Comparing the TC17 model (green) with the older, ejecta-dominated light curve models (blue). Each panel represents the parameter value combinations from Table 2. See Appendix A for details. This figure does not include data for SN 2022esa.

3.3 is because at high densities, the onset of the Sedov phase is occurring before the light curve becomes optically thin to free-free absorption. The Sedov solution has a higher rate of deceleration than the ejecta-dominated phase, so the decrease in the magnetic field and electron energy densities (that power the synchrotron emission) is occurring faster. By the time the light curve emerges from free-free absorption therefore, the luminosity has already significantly decreased compared to the ejecta-dominated case, giving an overall fainter light curve in the TC17 models.

In Figure 6, we see the difference between the two models in the range of mass-loss rates ruled out by observations. The difference in the lower end of the ruled out range between the two models is minor (~ 0.1 dex, the largest being 0.4 dex in SN 2002ic for $\epsilon_B = 0.01$, $T_{wind} = 2 \times 10^4$ K), caused mainly by the slightly steeper slope of the light curve in the ST phase for mass-loss rates approaching $10^{-3} \text{ M}_{\odot} \text{ yr}^{-1}$ (100 km s^{-1}) $^{-1}$. We see a more noticeable difference between the two models for the upper end of the ruled-out range (with TC17 on average being 0.4 dex lower, the largest being 0.7 dex in SN 1999E). This difference gets larger for older SNe because the light curves of the “old” model get brighter with mass-loss rate, and so a larger extent (in mass-loss rate) of the light curve can be excluded by the upper limit (Figure 3). Additionally, the time when $\tau_{ff} \gtrsim 1$ is prolonged for the TC17 model because of the slower evolution of the shock, further restricting the upper limit that can be constrained.

REFERENCES

- Aldering, G., Antilogus, P., Bailey, S., et al. 2006, *ApJ*, 650, 510, doi: [10.1086/507020](https://doi.org/10.1086/507020)
- Astropy Collaboration, Price-Whelan, A. M., Lim, P. L., et al. 2022, *ApJ*, 935, 167, doi: [10.3847/1538-4357/ac7c74](https://doi.org/10.3847/1538-4357/ac7c74)
- Bietenholz, M. F., Bartel, N., Argo, M., et al. 2021, *ApJ*, 908, 75, doi: [10.3847/1538-4357/abccd9](https://doi.org/10.3847/1538-4357/abccd9)
- Blondin, S., & Tonry, J. L. 2007, *ApJ*, 666, 1024, doi: [10.1086/520494](https://doi.org/10.1086/520494)
- Bochenek, C. D., Dwarkadas, V. V., Silverman, J. M., et al. 2018, *MNRAS*, 473, 336, doi: [10.1093/mnras/stx2029](https://doi.org/10.1093/mnras/stx2029)
- Bradley, L., Sipőcz, B., Robitaille, T., et al. 2023, *astropy/photutils*: 1.9.0, 1.9.0, Zenodo, Zenodo, doi: [10.5281/zenodo.8248020](https://doi.org/10.5281/zenodo.8248020)
- Burns, C. R., Parent, E., Phillips, M. M., et al. 2018, *ApJ*, 869, 56, doi: [10.3847/1538-4357/aae51c](https://doi.org/10.3847/1538-4357/aae51c)
- CASA Team, Bean, B., Bhatnagar, S., et al. 2022, *PASP*, 134, 114501, doi: [10.1088/1538-3873/ac9642](https://doi.org/10.1088/1538-3873/ac9642)
- Chandra, P. 2018, *SSRv*, 214, 27, doi: [10.1007/s11214-017-0461-6](https://doi.org/10.1007/s11214-017-0461-6)
- Chevalier, R. A. 1982, *ApJ*, 258, 790, doi: [10.1086/160126](https://doi.org/10.1086/160126)
- . 1998, *ApJ*, 499, 810, doi: [10.1086/305676](https://doi.org/10.1086/305676)
- Chevalier, R. A., & Fransson, C. 2006, *ApJ*, 651, 381, doi: [10.1086/507606](https://doi.org/10.1086/507606)
- Chevalier, R. A., & Fransson, C. 2017, *Handbook of Supernovae*, 875, doi: [10.1007/978-3-319-21846-5_34](https://doi.org/10.1007/978-3-319-21846-5_34)
- Chevalier, R. A., Fransson, C., & Nymark, T. K. 2006, *ApJ*, 641, 1029, doi: [10.1086/500528](https://doi.org/10.1086/500528)
- Chomiuk, L., & Wilcots, E. M. 2009, *ApJ*, 703, 370, doi: [10.1088/0004-637X/703/1/370](https://doi.org/10.1088/0004-637X/703/1/370)
- Chomiuk, L., Krauss, M. I., Rupen, M. P., et al. 2012a, *ApJ*, 761, 173, doi: [10.1088/0004-637X/761/2/173](https://doi.org/10.1088/0004-637X/761/2/173)
- Chomiuk, L., Soderberg, A. M., Moe, M., et al. 2012b, *ApJ*, 750, 164, doi: [10.1088/0004-637X/750/2/164](https://doi.org/10.1088/0004-637X/750/2/164)
- Chomiuk, L., Soderberg, A. M., Chevalier, R. A., et al. 2016, *ApJ*, 821, 119, doi: [10.3847/0004-637X/821/2/119](https://doi.org/10.3847/0004-637X/821/2/119)
- Chugai, N. N. 1991, *MNRAS*, 250, 513, doi: [10.1093/mnras/250.3.513](https://doi.org/10.1093/mnras/250.3.513)
- Darnley, M. J., Hounsell, R., O’Brien, T. J., et al. 2019, *Nature*, 565, 460, doi: [10.1038/s41586-018-0825-4](https://doi.org/10.1038/s41586-018-0825-4)
- Dewdney, P. E., Hall, P. J., Schilizzi, R. T., & Lazio, T. J. L. W. 2009, *IEEE Proceedings*, 97, 1482, doi: [10.1109/JPROC.2009.2021005](https://doi.org/10.1109/JPROC.2009.2021005)
- Dilday, B., Howell, D. A., Cenko, S. B., et al. 2012, *Science*, 337, 942, doi: [10.1126/science.1219164](https://doi.org/10.1126/science.1219164)
- Dwarkadas, V. V. 2023, *MNRAS*, 520, 1362, doi: [10.1093/mnras/stac3384](https://doi.org/10.1093/mnras/stac3384)
- . 2024, *MNRAS*, 533, 27, doi: [10.1093/mnras/stae1628](https://doi.org/10.1093/mnras/stae1628)
- Fox, O. D., Silverman, J. M., Filippenko, A. V., et al. 2015, *MNRAS*, 447, 772, doi: [10.1093/mnras/stu2435](https://doi.org/10.1093/mnras/stu2435)
- Fransson, C., Lundqvist, P., & Chevalier, R. A. 1996, *ApJ*, 461, 993, doi: [10.1086/177119](https://doi.org/10.1086/177119)
- Graham, M. L., Harris, C. E., Fox, O. D., et al. 2017, *ApJ*, 843, 102, doi: [10.3847/1538-4357/aa78ee](https://doi.org/10.3847/1538-4357/aa78ee)
- Graham, M. L., Harris, C. E., Nugent, P. E., et al. 2019, *ApJ*, 871, 62, doi: [10.3847/1538-4357/aaf41e](https://doi.org/10.3847/1538-4357/aaf41e)
- Hallinan, G., Ravi, V., Weinreb, S., et al. 2019, in *Bulletin of the American Astronomical Society*, Vol. 51, 255, doi: [10.48550/arXiv.1907.07648](https://doi.org/10.48550/arXiv.1907.07648)
- Hamuy, M., Phillips, M. M., Suntzeff, N. B., et al. 2003, *Nature*, 424, 651, doi: [10.1038/nature01854](https://doi.org/10.1038/nature01854)
- Han, Z., & Podsiadlowski, P. 2006, *MNRAS*, 368, 1095, doi: [10.1111/j.1365-2966.2006.10185.x](https://doi.org/10.1111/j.1365-2966.2006.10185.x)
- Harris, C. E., Chomiuk, L., & Nugent, P. E. 2021, *ApJ*, 912, 23, doi: [10.3847/1538-4357/abe940](https://doi.org/10.3847/1538-4357/abe940)
- Harris, C. E., Nugent, P. E., & Kasen, D. N. 2016, *ApJ*, 823, 100, doi: [10.3847/0004-637X/823/2/100](https://doi.org/10.3847/0004-637X/823/2/100)
- Harris, C. E., Sarbadhicary, S. K., Chomiuk, L., et al. 2023, *ApJ*, 952, 24, doi: [10.3847/1538-4357/acd84f](https://doi.org/10.3847/1538-4357/acd84f)
- Harris, C. E., Nugent, P. E., Horesh, A., et al. 2018, *ApJ*, 868, 21, doi: [10.3847/1538-4357/aae521](https://doi.org/10.3847/1538-4357/aae521)
- Harris, C. R., Millman, K. J., van der Walt, S. J., et al. 2020, *Nature*, 585, 357, doi: [10.1038/s41586-020-2649-2](https://doi.org/10.1038/s41586-020-2649-2)
- Horesh, A., Kulkarni, S. R., Fox, D. B., et al. 2012, *ApJ*, 746, 21, doi: [10.1088/0004-637X/746/1/21](https://doi.org/10.1088/0004-637X/746/1/21)
- Hosseinizadeh, G., Sand, D. J., Sarbadhicary, S. K., et al. 2023, *ApJL*, 953, L15, doi: [10.3847/2041-8213/ace7c0](https://doi.org/10.3847/2041-8213/ace7c0)
- Hunter, J. D. 2007, *Computing in Science & Engineering*, 9, 90, doi: [10.1109/MCSE.2007.55](https://doi.org/10.1109/MCSE.2007.55)
- Iben, I., J., & Tutukov, A. V. 1984, *ApJS*, 54, 335, doi: [10.1086/190932](https://doi.org/10.1086/190932)
- Inserra, C., Fraser, M., Smartt, S. J., et al. 2016, *MNRAS*, 459, 2721, doi: [10.1093/mnras/stw825](https://doi.org/10.1093/mnras/stw825)
- Jha, S. W., Maguire, K., & Sullivan, M. 2019, *Nature Astronomy*, 3, 706, doi: [10.1038/s41550-019-0858-0](https://doi.org/10.1038/s41550-019-0858-0)
- Katsuda, S., Mori, K., Maeda, K., et al. 2015, *ApJ*, 808, 49, doi: [10.1088/0004-637X/808/1/49](https://doi.org/10.1088/0004-637X/808/1/49)
- Kool, E. C., Johansson, J., Sollerman, J., et al. 2023, *Nature*, 617, 477, doi: [10.1038/s41586-023-05916-w](https://doi.org/10.1038/s41586-023-05916-w)
- Leloudas, G., Hsiao, E. Y., Johansson, J., et al. 2015, *A&A*, 574, A61, doi: [10.1051/0004-6361/201322035](https://doi.org/10.1051/0004-6361/201322035)
- Liu, Z.-W., Röpke, F. K., & Han, Z. 2023, *Research in Astronomy and Astrophysics*, 23, 082001, doi: [10.1088/1674-4527/acd89e](https://doi.org/10.1088/1674-4527/acd89e)
- Livio, M., & Riess, A. G. 2003, *ApJL*, 594, L93, doi: [10.1086/378765](https://doi.org/10.1086/378765)
- Lundqvist, P., Mattila, S., Sollerman, J., et al. 2013, *MNRAS*, 435, 329, doi: [10.1093/mnras/stt1303](https://doi.org/10.1093/mnras/stt1303)

- Lundqvist, P., Kundu, E., Pérez-Torres, M. A., et al. 2020, *ApJ*, 890, 159, doi: [10.3847/1538-4357/ab6dc6](https://doi.org/10.3847/1538-4357/ab6dc6)
- Marcowith, A., Bret, A., Bykov, A., et al. 2016, *Reports on Progress in Physics*, 79, 046901, doi: [10.1088/0034-4885/79/4/046901](https://doi.org/10.1088/0034-4885/79/4/046901)
- Matteucci, F., & Recchi, S. 2001, *ApJ*, 558, 351, doi: [10.1086/322472](https://doi.org/10.1086/322472)
- McMullin, J. P., Waters, B., Schiebel, D., Young, W., & Golap, K. 2007, in *Astronomical Society of the Pacific Conference Series*, Vol. 376, *Astronomical Data Analysis Software and Systems XVI*, ed. R. A. Shaw, F. Hill, & D. J. Bell, 127
- Mo, G., De, K., Wiston, E., et al. 2025, *ApJL*, 980, L33, doi: [10.3847/2041-8213/adaf92](https://doi.org/10.3847/2041-8213/adaf92)
- Moore, K., & Bildsten, L. 2012, *ApJ*, 761, 182, doi: [10.1088/0004-637X/761/2/182](https://doi.org/10.1088/0004-637X/761/2/182)
- Murphy, E. J., Bolatto, A., Chatterjee, S., et al. 2018, in *Astronomical Society of the Pacific Conference Series*, Vol. 517, *Science with a Next Generation Very Large Array*, ed. E. Murphy, 3, doi: [10.48550/arXiv.1810.07524](https://doi.org/10.48550/arXiv.1810.07524)
- Nadezhin, D. K. 1985, *Ap&SS*, 112, 225, doi: [10.1007/BF00653506](https://doi.org/10.1007/BF00653506)
- Nomoto, K. 1982, *ApJ*, 253, 798, doi: [10.1086/159682](https://doi.org/10.1086/159682)
- Panagia, N., Van Dyk, S. D., Weiler, K. W., et al. 2006, *ApJ*, 646, 369, doi: [10.1086/504710](https://doi.org/10.1086/504710)
- Perlmutter, S., Aldering, G., Goldhaber, G., et al. 1999, *ApJ*, 517, 565, doi: [10.1086/307221](https://doi.org/10.1086/307221)
- Phillips, M. M. 1993, *ApJL*, 413, L105, doi: [10.1086/186970](https://doi.org/10.1086/186970)
- Phillips, M. M., Lira, P., Suntzeff, N. B., et al. 1999, *AJ*, 118, 1766, doi: [10.1086/301032](https://doi.org/10.1086/301032)
- Pskovskii, I. P. 1977, *Soviet Ast.*, 21, 675
- Raiteri, C. M., Villata, M., & Navarro, J. F. 1996, *A&A*, 315, 105
- Reynolds, S. P., Williams, B. J., Borkowski, K. J., & Long, K. S. 2021, *ApJ*, 917, 55, doi: [10.3847/1538-4357/ac0ced](https://doi.org/10.3847/1538-4357/ac0ced)
- Riess, A. G., Filippenko, A. V., Challis, P., et al. 1998, *AJ*, 116, 1009, doi: [10.1086/300499](https://doi.org/10.1086/300499)
- Ruiter, A. J., & Seitzzahl, I. R. 2025, *A&A Rv*, 33, 1, doi: [10.1007/s00159-024-00158-9](https://doi.org/10.1007/s00159-024-00158-9)
- Salamanca, I., Cid-Fernandes, R., Tenorio-Tagle, G., et al. 1998, *MNRAS*, 300, L17, doi: [10.1046/j.1365-8711.1998.02093.x](https://doi.org/10.1046/j.1365-8711.1998.02093.x)
- Seaquist, E. R., Krogulec, M., & Taylor, A. R. 1993, *ApJ*, 410, 260, doi: [10.1086/172742](https://doi.org/10.1086/172742)
- Seaquist, E. R., & Taylor, A. R. 1990, *ApJ*, 349, 313, doi: [10.1086/168315](https://doi.org/10.1086/168315)
- Sedov, L. I. 1959, *Similarity and Dimensional Methods in Mechanics* (Academic Press)
- Sfaradi, I., Horesh, A., Fender, R., et al. 2025, *ApJ*, 979, 189, doi: [10.3847/1538-4357/ad9e93](https://doi.org/10.3847/1538-4357/ad9e93)
- Sharma, Y., Sollerman, J., Fremling, C., et al. 2023, *ApJ*, 948, 52, doi: [10.3847/1538-4357/acbc16](https://doi.org/10.3847/1538-4357/acbc16)
- Shen, K. J., Kasen, D., Miles, B. J., & Townsley, D. M. 2018, *ApJ*, 854, 52, doi: [10.3847/1538-4357/aaa8de](https://doi.org/10.3847/1538-4357/aaa8de)
- Silverman, J. M., Nugent, P. E., Gal-Yam, A., et al. 2013, *ApJS*, 207, 3, doi: [10.1088/0067-0049/207/1/3](https://doi.org/10.1088/0067-0049/207/1/3)
- Smith, N. 2014, *ARA&A*, 52, 487, doi: [10.1146/annurev-astro-081913-040025](https://doi.org/10.1146/annurev-astro-081913-040025)
- Soderberg, A. M., Chevalier, R. A., Kulkarni, S. R., & Frail, D. A. 2006, *ApJ*, 651, 1005, doi: [10.1086/507571](https://doi.org/10.1086/507571)
- Soderberg, A. M., Kulkarni, S. R., Berger, E., et al. 2005, *ApJ*, 621, 908, doi: [10.1086/427649](https://doi.org/10.1086/427649)
- Soderberg, A. M., Margutti, R., Zauderer, B. A., et al. 2012, *ApJ*, 752, 78, doi: [10.1088/0004-637X/752/2/78](https://doi.org/10.1088/0004-637X/752/2/78)
- Tang, X., & Chevalier, R. A. 2017, *MNRAS*, 465, 3793, doi: [10.1093/mnras/stw2978](https://doi.org/10.1093/mnras/stw2978)
- Taylor, G. I. 1946, *Proceedings of the Royal Society of London Series A*, 186, 273, doi: [10.1098/rspa.1946.0044](https://doi.org/10.1098/rspa.1946.0044)
- Terwel, J. H., Maguire, K., Dimitriadis, G., et al. 2025, *A&A*, 694, A11, doi: [10.1051/0004-6361/202348476](https://doi.org/10.1051/0004-6361/202348476)
- Thompson, T. A., Quataert, E., & Murray, N. 2009, *MNRAS*, 397, 1410, doi: [10.1111/j.1365-2966.2009.14889.x](https://doi.org/10.1111/j.1365-2966.2009.14889.x)
- Tutukov, A. V., & Yungelson, L. R. 1979, *AcA*, 29, 665
- Virtanen, P., Gommers, R., Oliphant, T. E., et al. 2020, *Nature Methods*, 17, 261, doi: [10.1038/s41592-019-0686-2](https://doi.org/10.1038/s41592-019-0686-2)
- Wang, L., Hu, M., Wang, L., et al. 2024, *Nature Astronomy*, 8, 504, doi: [10.1038/s41550-024-02197-9](https://doi.org/10.1038/s41550-024-02197-9)
- Webbink, R. F. 1984, *ApJ*, 277, 355, doi: [10.1086/161701](https://doi.org/10.1086/161701)
- Weiler, K. W., Panagia, N., Montes, M. J., & Sramek, R. A. 2002, *ARA&A*, 40, 387, doi: [10.1146/annurev.astro.40.060401.093744](https://doi.org/10.1146/annurev.astro.40.060401.093744)
- Whelan, J., & Iben, Icko, J. 1973, *ApJ*, 186, 1007, doi: [10.1086/152565](https://doi.org/10.1086/152565)
- Wood-Vasey, W. M., & Sokoloski, J. L. 2006, *ApJL*, 645, L53, doi: [10.1086/506179](https://doi.org/10.1086/506179)
- Yang, X., Liu, Z., Shan, H., et al. 2023, *The Astronomer's Telegram*, 16080, 1